ROYAL SOCIETY OF CHEMISTRY

PAPER

Hydrogen adsorption trends on two metal-doped Ni₂P surfaces for optimal catalyst design

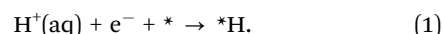Lauri Partanen, [iD] Simon Alberti [iD] and Kari Laasonen [iD] *

In this study, we looked at the hydrogen evolution reaction on the doubly doped Ni_3P_2 terminated Ni_2P surface. Two Ni atoms in the first three layers of the Ni_2P surface model were exchanged with two transition metal atoms. We limited our investigation to combinations of Al, Co, and Fe based on their individual effectiveness as Ni_2P dopants in our previous computational studies. The DFT calculated hydrogen adsorption free energy was employed as a predictor of the materials' catalytic HER activity. Our results indicate that the combination of Co and Fe dopants most improves the catalytic activity of the surface through the creation of multiple novel and active catalytic sites.
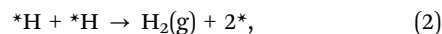
1 Introduction

The steady increase in energy demand caused by technological advances and population growth is one of the principal challenges facing the scientific community.[1–3] To exacerbate this issue, our reliance on fossil fuel combustion is unsustainable in the long run due to its limited availability and detrimental effects on the environment, climate, and human health.[2,4] Hence, current energy research focuses on finding new clean, secure, and sustainable sources of energy.

Viable large-scale energy alternatives to fossil fuels include nuclear and solar energies. For nuclear energy, long-term storage of highly toxic nuclear waste is an issue, as are the general risks associated with nuclear power plants.[5] On the other hand, solar energy is only intermittently available and requires a long term storage solution. One possibility would be to store the energy chemically as hydrogen, which is abundant, lightweight, and produces only water upon oxidation.[6] The large-scale conversion of energy to hydrogen could be accomplished by water-splitting through electrolysis. With this effective storage mechanism, solar energy could meet the global energy demand in an environmentally sustainable manner.
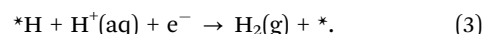
Electrochemical water-splitting consists of two parts: The hydrogen evolution reaction (HER) is a two-step process that takes place at the cathode, while the oxygen evolution reaction (OER) is a multistep process that occurs at the anode. Two HER pathways are normally considered, and the reaction mechanism depends on the pH of the electrolyte. Both mechanisms start with the Volmer reaction, where, in acidic conditions, the hydrogen first adsorbs on a surface site symbolised by *:

Department of Chemistry and Materials Science, Aalto University, P.O. Box 16100, FI-00076 Aalto, Finland. E-mail: kari.laasonen@aalto.fi

$$H^+(aq) + e^- + * \rightarrow *H. \qquad (1)$$

This can be followed by two adsorbed hydrogens joining together in the Tafel reaction

$$*H + *H \rightarrow H_2(g) + 2*, \qquad (2)$$

or by the arrival of a second proton directly from the solution in the Heyrovsky reaction

$$*H + H^+(aq) + e^- \rightarrow H_2(g) + *. \qquad (3)$$

Whether the reaction takes place in an alkaline or acidic medium, an efficient and cheap catalyst is required. Unfortunately, the best HER catalysts currently contain platinum, an exiguous noble metal.[3] This is partly why large-scale hydrogen production through reactions (1), (2), and (3) is not economically feasible. Consequently, recent studies have looked at non-precious compounds as more convenient replacements for platinum, with examples ranging from heteroatom-doped nano-carbons to transition metal chalcogenides, nitrides, carbides, selenides, phosphides, borides, and sulfides.[7–12] Particularly nickel phosphides have emerged as robust and efficient catalysts,[13,14] showing advantages in terms of synthesis routes, anti-corrosion features, electronic properties, and catalytic activities – especially in the acidic medium.[15–17]

Once an efficient catalytic material like Ni_2P has been identified, it is possible to further enhance its electrocatalytic performance through either morphological control or heteroatom doping.[18] For example, transition metal doping of Ni_2P structures by Mo,[19] Al,[20] Mn,[21] W,[22] V,[23,24] Co[25–27] and Fe[28–31] has already been experimentally verified to improve HER activity. Density functional studies have confirmed that the H-adsorption strength in the Volmer step depends on the microscopic structure of the surface and that dopants like Al, Mg, Cu, Co, Fe, Mo, and V can enhance the catalytic activity.[32,33]

Recently, experimentalists have begun to investigate the effect of incorporating multiple dopants on the Ni_2P surface with promising results.[31] To support these efforts, in this study, we consider the co-doping of the Ni_2P surface by two of the metals Fe, Co and Al. These three metals were chosen based on their individual effectiveness as dopants in our previous DFT studies[32,33] to keep the number of investigated surface structures manageable. We also manage the computational effort by using the broadly applied hydrogen adsorption free energy (ΔG_H) model[34–37] to evaluate the catalytic activity. In this model, $\Delta G_H \approx 0$ between the electrode surface and a molecular $H_2(g)$ reference indicates optimal HER activity according to Sabatier's principle.[36] As factors like the choice of the DFT functional can affect the ΔG_H values,[32] sites with $|\Delta G_H| < 0.1$ eV are considered optimal.[36] We focus exclusively on the Ni_3P_2 termination of the (0001) Ni_2P surface as it is the preferred bulk-like termination within the Ni_2P stability region[38,39] and is thought to be the active surface in Ni_2P nanowires.[40] Our main goals are to investigate how the combination of dopants alters the surface structure and how having multiple types of dopants impacts the HER activity of Ni_2P.

2 Systems and methods

2.1 Computational details

All DFT calculations were performed using the CP2K/QUICK-STEP software.[41,42] We made use of the Perdew–Burke–Ernzerhof (PBE) functional[43] with the Kohn–Sham orbitals expanded in a molecularly optimised double-valence polarised basis set (MOLOPT-SR-DZVP) and the core electrons represented by the Goedecker–Teter–Hutter pseudopotentials (GTH).[44–46] The plane-wave kinetic energy cutoff was set to 700 Ry, while the cutoff for the reference grid was 60 eV. Atomic positions were optimised with the force convergence criterion left to its default value of 0.023 eV Å^{-1}. Periodic boundary conditions were used to solve the Poisson equation for the electrostatic potential.

The Ni_2P bulk lattice parameters were obtained by allowing a supercell of $4 \times 4 \times 4$ unit cells to relax under a pressure tolerance of 0.1 kbar.[32] This resulted in a nonferromagnetic end-state with cell parameters $a = b = 5.860$ Å, and $c = 3.332$ Å. To obtain the atomic reference energies of Ni, Fe, Co, and Al in the crystalline phase, we employed a supercell of $10 \times 10 \times 10$ units with the PBE lattice parameters taken from the literature.[47–49]

While our original Ni_2P calculation employed the orbital transformation method, the reference energy calculations used the diagonalisation method with the Fermi temperature set to 75 K. When we studied the effect of increasing this temperature to 300 and 400 K, the impact on the energy/atom was less than 0.02 eV in all cases.[33]

Our surface calculations used the same diagonalisation method as our atomic reference calculations with a 75 K electronic smearing but added the Grimme D3(BJ) dispersion corrections.[50,51] We focused on the Ni_3P_2 termination of the (0001) Ni_2P surface because it seems to be the active surface in

Ni_2P nanowires[40] and also the preferred bulk-like termination in the Ni_2P stability region.[38,39] At around pH = 0, corresponding to the typical experimental conditions for HER in acid, this surface phase dominates at potentials $U > -0.21$ V vs. the standard hydrogen electrode.[52] Below this region, both experimental and computational studies find that the surface becomes enriched by phosphorus.[38,52–58] The resulting Ni_3P_2 + P termination then predominates within -0.21 V $\geq U \geq -0.36$ V. We chose not to include the Ni_3P_2 + P termination in this work because the pristine Ni_3P_2 + P surface is already such an efficient HER catalyst that it is difficult to detect any advantages of doping with the employed ΔG_H model.[33] Finally, for $U < -0.36$ V, the pristine Ni_3P_2 surface becomes passivated by H atoms attaching to the Ni_3 hollow sites.[52]

We modelled our surface with a seven-layer deep symmetric slab where the atoms at the bottom layer were fixed to their bulk positions.[32] As illustrated in Fig. 1, the Ni_3P_2 terminated Ni_2P surface has alternating Ni_3P_2 and Ni_3P layers.[59,60] Nanostructures such as terraces were not investigated. The dopant atoms were restricted to the top three layers, with only one dopant atom of each kind present in each surface. The notation $(M_1, M_2)(lx_1, lx_2)$ is used to distinguish the surfaces, where x_i is the layer of the dopant M_i with $x_i \in \{1, 2, 3\}$. The positions within a layer are described separately after the classification – when relevant. Since the first metal atom in (M_1, M_2) always occupies position 1 within its layer, only the second atom's position is provided. This convention is used because all the Ni positions within a given layer are equal in the pristine surface.

In all our calculations with this system, $5 \times 5 \times 1$ Monkhorst–Pack k-points were used. The simulation cell contained at least 10 Å of vacuum on both sides of the slab so that the total amount
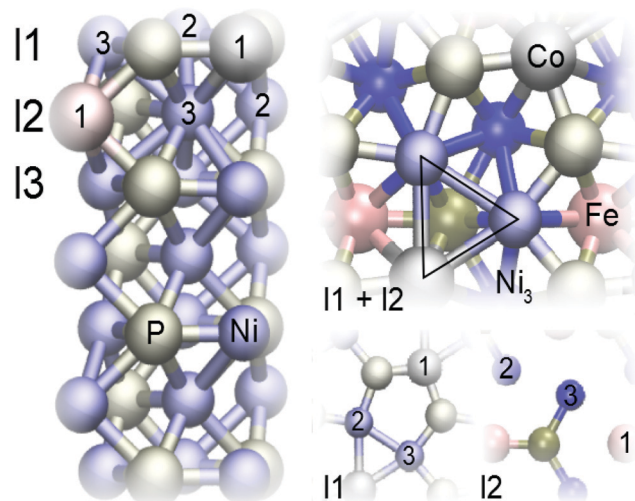

Fig. 1 The Ni_3P_2 terminated Ni_2P model system. In the depicted surface, the first layer is doped by a cobalt atom and the second by iron, corresponding to a (Co, Fe) (l1, l2) doping scheme. The whole slab structure is shown on the left, while the panels on the right provide a top view of the two highest layers (l1 + l2) and of the two layers separately (l1 and l2).

This journal is © the Owner Societies 2021

Phys. Chem. Chem. Phys., 2021, **23**, 11538–11547 | **11539**

of vacuum between adjacent surface images was always more than 20 Å. As Hakala and Laasonen[32] found that increasing the supercell surface area had no effect on the H-adsorption energies, its impact was not studied here. They also showed that while a change from the PBE to the RPBE functional[61] slightly weakened H binding, the turning off of the van der Waals interaction had a minuscule effect on the ΔG_H values.[32]

2.2 HER activity model

Our analysis was based on the simple kinetic model proposed by Nørskov *et al.*[34,35] that links the differential H-adsorption Gibbs free energy with the exchange current density. In this model, the relevant H coverage at a hydrogen chemical potential μ is determined from the minimum of the total adsorption energy $\Delta_{tot}G_H(n)$:

$$\Delta_{tot}G_H(n) = G(n) - G(0) - n\mu \qquad (4)$$

where $G(n)$ is the free energy of the surface with n hydrogen atoms attached and $G(0)$ is the free energy of the bare surface. The chemical potential is calculated from the free energy of molecular hydrogen in the gas phase, $G(H_2)$, with[37]

$$\mu = \frac{1}{2}G(H_2) - eU \qquad (5)$$

where U is the cathode potential.

Adsorption sites are compared based on their differential Gibbs free energies of adsorption

$$\Delta G_H(n) = G(n) - G(n-1) - \mu. \qquad (6)$$

In practice, this quantity is calculated from

$$\Delta G_H(n) = E(n) - E(n-1) - \frac{1}{2}E(H_2) + 0.24 \text{ eV} + eU \qquad (7)$$

where a factor of 0.24 eV is employed to account for the differences in zero-point energies and entropies between the products and reactants at pH = 0.[34,35,37] $E(n)$ is the total energy of the surface at 0 K with n hydrogen atoms attached. It can be obtained directly from DFT calculations. Only the neutral states (*i.e.*, $U = 0$ V) were considered in this study since test calculations for charged pristine and Al-doped surfaces failed to demonstrate any charge trapping.[32] One should also note that $\Delta G_H(n)$ is a purely thermodynamic indicator of the HER activity, so it neglects any activation energy barriers in the system.[62]

Once the differential Gibbs free energy is known for several surface sites, the minimum overpotential to adsorb hydrogen at a hydrogen coverage n is

$$\eta(n) = \frac{\min \Delta G_H(n)}{e} \qquad (8)$$

where the minimum is taken over the surface sites. We used 14 starting positions for each added hydrogen, increasing the coverage until the $\Delta G_H(n)$ value became positive. The minimum $\Delta G_H(n)$ values for a given coverage were then used to compare and understand the surfaces through Sabatier's principle: If $\Delta G_H < 0$, hydrogen binds too strongly to the surface, and there is a lack of available sites for H + H recombination. If $\Delta G_H > 0$, hydrogen binds too weakly, and proton transfer

becomes progressively more difficult with increasing ΔG_H as hydrogen becomes unstable on the surface.[35]

3 Results and discussion

3.1 Doping energies

Fig. 2 displays the single-atom doping energies of Co, Fe, and Al for the three topmost layers. These values have been taken from our previous studies[32,33] to facilitate the interpretation of the doping energies of the (Al, Fe), (Al, Co), and (Co, Fe) co-doped surfaces. Meanwhile, the two-atom doping energies for the three topmost layers of Ni_2P with Co and Fe are shown in Fig. 3, with sample structures included. The doping energy is calculated as the energy of the optimised doped slab minus the reference doping energy. This reference was obtained from the pristine slab's energy by subtracting the atomic energies of two Ni atoms and adding the atomic energies of the two dopants. All atomic energies were calculated from the stable crystal structures as described in Section 2.1. An analogous process was used to calculate the single-atom doping energies in Fig. 2.

It seems that the doping energy in Fig. 3 is almost exclusively determined by the layer of the dopant atoms, as the energies remain almost identical when the position of the iron dopant is modified within a layer. The energy is also seen to decrease the deeper the atoms are, indicating that the dopant atoms would not aggregate on the material's surface but rather a few layers down.

An interesting feature of Fig. 3 is that the decrease in energy for both Co and Fe as one moves down in layers appears almost linear. This is reflected in Fig. 2, where the single-atom doping energy decreases fairly linearly for Co and Fe. Indeed, for most cases in Fig. 3, one can predict the doping energies to less than 0.1 eV just by adding the single-doping energies of Fig. 2 together. This implies minimal cooperation effects between the two dopants.

Similarly to Fig. 3, Fig. 4 and 5 contain the doping energies for the (Co, Al) and (Al, Fe) systems. As in the (Co, Fe) case, the
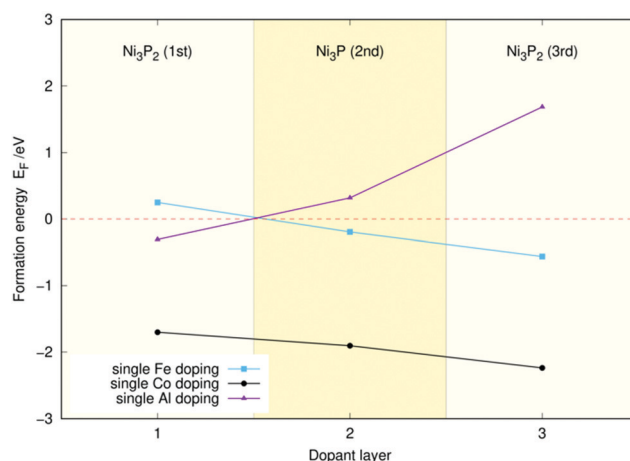

Fig. 2 Single-atom doping energies (E_F) for Fe, Co, and Al for the three topmost layers of the Ni_3P_2 termination of Ni_2P.

11540 | *Phys. Chem. Chem. Phys.*, 2021, **23**, 11538–11547

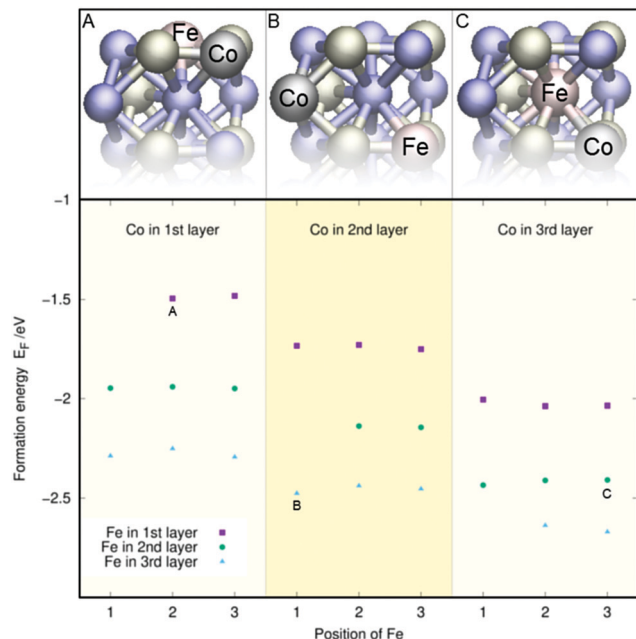This journal is © the Owner Societies 2021

Fig. 3 Two-atom doping energies (E_F) for Co and Fe for the top three layers of the Ni_3P_2 termination of Ni_2P. Panels A, B, and C provide sample geometries for their respective data points.

Fig. 5 Two-atom doping energies (E_F) for Al and Fe for the three topmost layers of the Ni_3P_2 termination of Ni_2P.

energy is mostly unaffected by the dopant's position in a given layer for both metal combinations. Furthermore, Co and Fe follow the same trends as they did before: The energy of the system decreases the lower the layer of the Co or Fe dopant. Aluminium follows the opposite trend: Its doping energy is at the lowest in layer one and increases significantly for the two subsequent layers. For both figures, the energies largely follow the linear trends predicted from Fig. 2. The only exception to this in Fig. 5 is the (Al, Fe) (l3, l2) doping scheme with Fe at the 2nd position. There, the substantial energy difference arises from a restructuring of the surface. Similar anomalies caused by surface reconstructions were occasionally observed in our single dopant study.[33] Regardless, the doping energies can
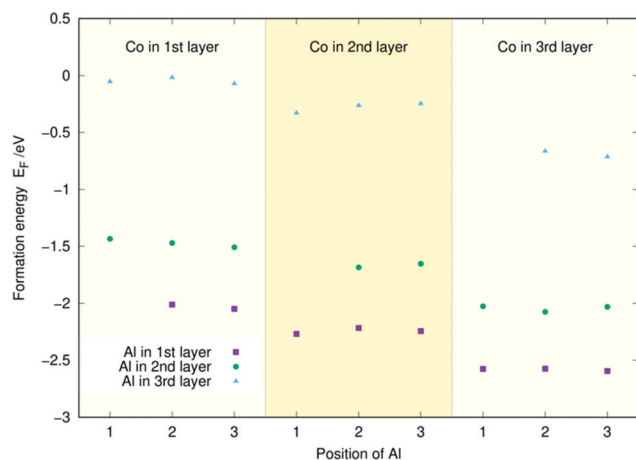
almost always be predicted to an accuracy of 0.1 eV using the individual atom doping energies from Fig. 2, as in the (Co, Fe) case. Thus, the coordination effects appear small also for the (Co, Al) and (Al, Fe) surfaces.

3.2 Hydrogen adsorption free energies

First adsorption free energies. The first hydrogen adsorption energies calculated with eqn (7) are reported in Fig. 6. In these calculations, a hydrogen atom was placed in one of fourteen random locations above the surface, followed by a geometry optimisation as described in Section 2.2. Fig. 6 shows the lowest adsorption free energies from these fourteen calculations. The dopant metal combination is indicated by the shape of the data point, whereas its colour indicates the second dopant's position within a layer. The layers of the dopants are shown on the horizontal axis. The effect of dopant positions on the

Fig. 4 Two-atom doping energies (E_F) for Co and Al for the three topmost layers of the Ni_3P_2 termination of Ni_2P.
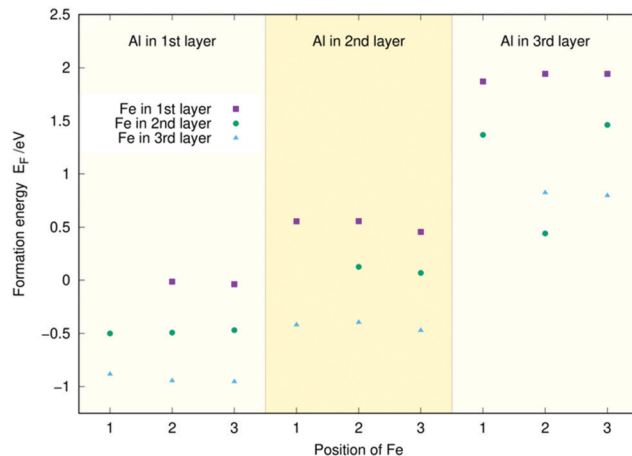

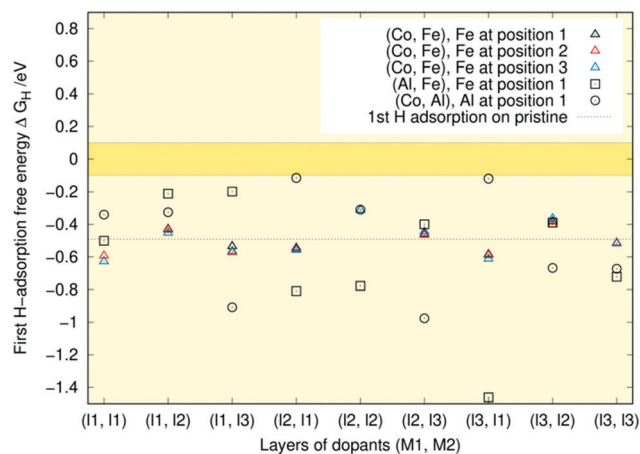Fig. 6 First hydrogen adsorption free energies (ΔG_H) for singly (Co, Fe), (Co, Al), and (Al, Fe) -doped Ni_2P respectively in layers (l1, l2). Colours indicate different positions within a given layer for the (Co, Fe) case. The deep yellow band highlights the ± 0.1 eV region around the optimal $\Delta G_H = 0$ eV value. The pristine value is indicated by a dashed black line for comparison.

adsorption free energy was only studied for the (Co, Fe)-doped surface due to its minimal impact on the doping energy.

The central message from Fig. 6 is that all the data lie below the optimal range of ± 0.1 eV. This indicates that with little previous H-coverage, the surface binds hydrogen too strongly for HER to occur effectively. There is considerable variation in the first adsorption free energy for the Al-containing doping schemes with some structures right at the border of the optimal range and others like (Al, Fe) (l3, l1) more than twice lower in energy than the pristine case. The first adsorption free energies are closest to optimal when aluminium is present in the first layer and the second dopant is in some other layer. If both dopants are in the first layer, the free energy is lower. These findings line up with our previous results where single Al doping of the topmost Ni_3P_2 layer resulted in a free energy of -0.02 eV, whereas on a triply Al-doped surface layer, the free energy decreased to -0.37 eV.[32] The lower adsorption free energies are generally encountered when aluminium is not in the topmost layer. Meanwhile, the (Co, Fe) free energies show trends similar to those observed in our recent doping study,[33] as all energies remain relatively close to the pristine one. Comparing the coloured symbols' locations, we see that changing the dopant position within a layer has little impact on the adsorption free energy, as expected.

In line with previous studies,[32,33,52,63] the Ni_3 hollow site depicted in Fig. 1 and various bridge sites predominated the adsorption geometries: In 19 out of the studied 42 surfaces, the first hydrogen was found in the Ni_3 deep site. In an equal number of cases, the hydrogen ended up on one of the edges of the Ni_3 site. These bridge configurations were commonplace when the dopants were located in the top two layers, as expected based on the finding that in low doping conditions, hollow site adsorption is most perturbed by substitutional doping of the first layer.[33] Indeed, Hakala and Laasonen[32] observed that low Al doping of the surface layer weakened the hollow site's binding energy, resulting in H coordination by the two Ni atoms. When Al was located in the third layer, we occasionally observed a restructuring of the surface in which one of the P atoms lifted about 1 Å from the topmost Ni_3P_2-layer, attaching to the hydrogen. Model cases for the two prevailing adsorption patterns are shown in Fig. 7.
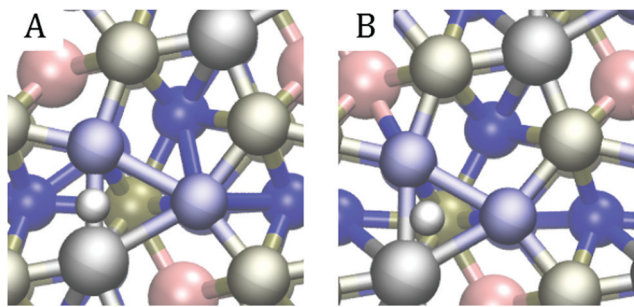
Second adsorption free energies. The adsorption free energies for the second hydrogen adsorption are shown in Fig. 8. These were obtained by taking the lowest free-energy structure from Fig. 6, adding a second hydrogen atom to each of the 14 starting locations of the first calculation, and optimising the geometry. Analogously to Fig. 6, the symbols represent the lowest ΔG_H values for the second hydrogen adsorption. The shape of the symbols indicates the doping scheme, and its colour the position of the dopants. The layers of the dopants are listed on the horizontal axis. An open symbol is used when less than two unique adsorption geometries lie within the optimal region, whereas a full symbol indicates that the number of geometries within the ± 1 eV region was greater than two.

All metal combinations in Fig. 8 show structures where the second hydrogen adsorption falls within the ideal region and the free energies are naturally higher than the first adsorption free energies. When calculations with more than two hydrogens are included, approximately two-thirds of the adsorption sites are ideal for the (Co, Fe) surfaces. In contrast, for both (Al, Fe) and (Co, Al), the adsorption free energy of the second hydrogen is in many cases already too high, indicating that the hydrogen does not stick to the surface. Only the iron and cobalt doped surfaces possess plenty of adsorption geometries in the optimal region. This provides another computational verification of the experimental results that both Fe and Co doping can enhance catalytic activity.[25–31,64–73] One reason behind this might be that the surface provides partially positive Ni–Co–Fe metal centres and partially negative P sites that act as hydride and proton acceptors, respectively. On the other hand, the Ni d^8 electron contribution to the metallic bands is perhaps too much above the optimal chemisorption of H^+.[66] The shift in the d-band centre with respect to the Fermi level caused by

Fig. 7 Sample adsorption patterns for the first hydrogen adsorption of the (Co, Al) (l1, l2) doping scheme: (A) Co–Ni bridge adsorption, (B) Ni_3 hollow site adsorption.

Fig. 8 Second hydrogen adsorption free energies (ΔG_H) for singly (Co, Fe), (Co, Al), and (Al, Fe)-doped Ni_2P respectively in layers (l1, l2). For the (Co, Fe) case, colours indicate different positions within a given layer. The deep yellow band highlights the ± 0.1 eV region around the optimal $\Delta G_H = 0$ eV value. The value for the pristine Ni_2P surface is indicated by a dashed red line for comparison. An open symbol implies that the number of unique adsorption geometries within the optimal region is less than two and a full symbol indicates that the number was two or more.

dopant atoms with fewer d-electrons can reduce the chemical interaction between the reaction intermediates and the catalyst surface.[13,18,66,74]

As was the case for the first hydrogen adsorption, the free energy seems almost independent of the atom's position within the layer. The only exceptions are the three doping schemes on the left of Fig. 8, where position three is somehow always lower in energy.

In all but one case, multiple bonding patterns exist within the ideal region. Six such patterns for (Co, Fe) (l1, l2) with the iron in the second position are illustrated in Fig. 9. Panel E shows the most common bonding pattern for (Co, Fe) where one of the hydrogens stays at the Ni_3 hollow site, and the other occupies a metal–phosphorus bridge site. Only one of the (Co, Fe) doping schemes within the ideal region did not feature this geometry. This is unsurprising, given that the same bonding pattern was found for the pristine surface by Liu and Rodriguez[63] and that it was also the most prevalent pattern observed in our previous study.[33] Even though the negatively partially charged phosphorus primarily attracts hydronium ions, it also participates in bonding hydrogen after the hydrogen atoms have poisoned the deep Ni_3-sites. This dual role of the P atoms results in an orbital environment that is more conducive for HER.

Besides the bridge – hollow site bonding pattern, we saw combinations of different bridge sites, as shown in panels B, C, D, and F of Fig. 9, and combinations of bridge site and single atom adsorptions. In a rare cases, even spontaneous hydrogen formation was observed, as in panel A. The same patterns are observed for (Co, Al) and (Al, Fe) and demonstrate the cornucopia of distinct and active catalytic sites available on these surfaces.

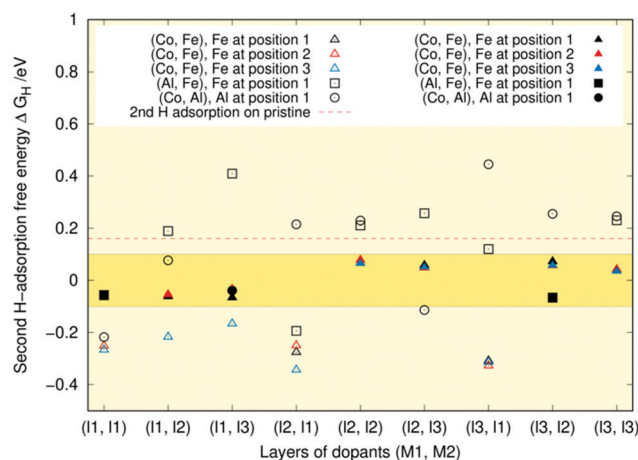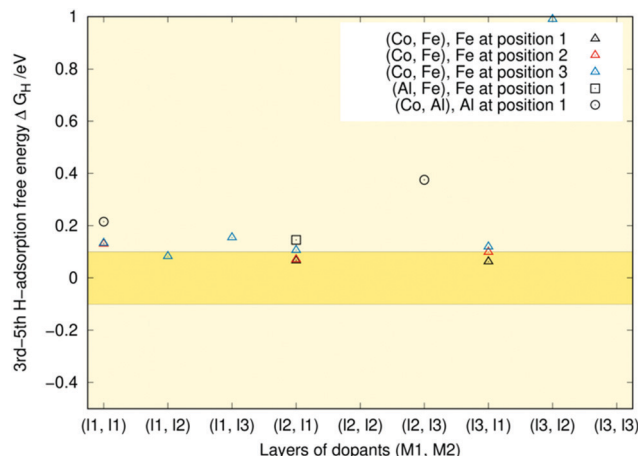Fig. 10 Third to fifth hydrogen adsorption free energies (ΔG_H) for singly (Co, Fe), (Co, Al), and (Al, Fe)-doped Ni_2P respectively in layers (l1, l2). Different positions within a given layer are indicated by colours for the (Co, Fe) case. The deep yellow band highlights the ± 0.1 eV region around the optimal $\Delta G_H = 0$ eV value.

Higher adsorption free energies. Fig. 10 shows the lowest obtained adsorption free energies above the lower threshold of the optimal region, i.e. -0.1 eV, for the cases where the first two adsorption free energies were below the optimal region. Interestingly, the number of adsorbed hydrogen varied significantly before this condition was met: for (Co, Al) (l1, l1) and (Al, Fe) (l2, l1), the figure shows the third adsorption free energy, whereas, for (Co, Al) (l2, l3) and (Co, Fe) (l1, l1), the fifth free energy is reported. The rest of the points correspond to the adsorption free energies of the fourth hydrogen.
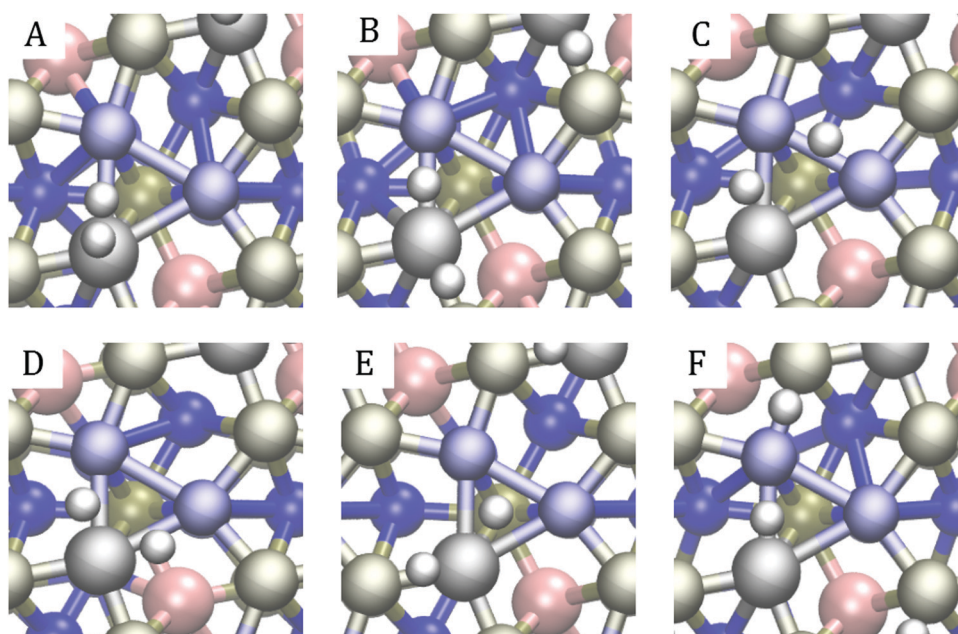

Fig. 9 Sample adsorption patterns for the second hydrogen adsorption for the (Co, Fe) (l1, l2) configuration with iron at the second position: (A) H_2 formation, (B) Ni–Co bridge, Co–P bridge, (C) Ni–Co bridge, Ni–Ni bridge, (D) two Ni–Co bridge, (E) Ni_3 hollow site, Co–P bridge, (F) Ni–Co bridge, Ni–P bridge.

In most cases, the higher adsorption free energies are above the optimal region. Even when they are not, only a single adsorption geometry lies within the optimal region, as shown by the lack of full symbols in Fig. 10. Apparently, as the H-coverage increases, the surface can no longer bind hydrogen effectively. For these geometries, a dopant atom on the first layer typically binds three of the hydrogen atoms. This structure is reminiscent of the P-adatom's adsorption pattern in the Ni_3P_2 + P termination of Ni_2P observed in previous studies.[32,33,52]

In summary, the Ni_3P_2-terminated Ni_2P surface contains several very strongly binding Ni_3-sites. Thus, some coverage seems necessary for the HER to proceed effectively. Once the deep sites have been poisoned by hydrogen atoms, the partially negatively charged phosphorus starts to participate in the bonding of hydrogen, creating a highly conducive orbital environment for HER. However, if the H-coverage increases too much, the surface becomes unable to bind hydrogen sufficiently strongly for effective H_2 formation.

The cobalt and iron co-doped surface appears most active of the three studied. This preference might arise because dopant atoms with fewer d-electrons can decrease the chemical interaction between the reaction intermediates and the catalyst surface, which could be too strong for Ni_2P alone.[13,18,66,74] Iron and cobalt are chemically more similar to nickel than aluminium is. Consequently, as the pristine Ni_2P surface is already relatively HER active, the presence of Al dopants might perturb the orbital environment too much and lead to the generally weaker chemical binding of the second hydrogen observed in Fig. 8.

4 Conclusions

In this study, we have investigated the hydrogen evolution reaction on Ni_3P_2 terminated Ni_2P surfaces with two different metal atom dopants. Based on our previous computational studies,[32,33] we focused on mixtures of Co, Fe, and Al. The catalytic HER activity was estimated using the hydrogen adsorption free energy, following the self-consistent scheme proposed by Nørskov et al.[34,35] In most cases, the adsorption free energy of the second hydrogen fell in the optimal region of $|\Delta G_H| < 0.1$ eV. This indicates that some H-coverage is needed to poison the strongly binding Ni_3 sites before the HER can proceed effectively. Of the three studied metal combinations, the Co and Fe co-doped surface emerged as the most active. The observed adsorption patterns were similar to those reported in the literature, with bridge and Ni_3 hollow site occupations predominating. We speculate that the success of the Co and Fe doped surface might lie in a favourable shift in the d-band centre relative to the Fermi level, caused by dopant atoms with fewer d-electrons. In contrast, the Al-atoms might perturb the already favourable electronic environment of Ni_2P slightly too much.

To study the stability of our materials, we investigated the formation energies of the doped surfaces. We predict that the surface should be readily dopable by all three mixtures. Al is most likely found on the surface for the top three layers,

whereas the material seems to increase in stability the deeper the Fe and Co atoms are located.

Overall, our DFT calculations predict that the co-doping of Ni_2P, especially with Co and Fe, will lead to stable surfaces with improved catalytic activity. It seems that the incorporation of two different types of effective dopant atoms can result in the formation of new types of active sites. Since a real co-doped Ni_2P surface would include similar types of active sites as the solely Co or Fe doped surfaces, the appearance of novel sites should further enhance the catalytic activity of the surface within the accuracy of the employed model.

Conflicts of interest

There are no conflicts to declare.

Acknowledgements

References

1 N. S. Lewis and D. G. Nocera, Powering the planet: Chemical challenges in solar energy utilization, *Proc. Natl. Acad. Sci. U. S. A.*, 2006, **103**, 15729–15735.
2 N. Armaroli and V. Balzani, Towards an electricity-powered world, *Energy Environ. Sci.*, 2011, **4**, 3193–3222.
3 Z. W. Seh, J. Kibsgaard, C. F. Dickens, I. Chorkendorff, J. K. Nørskov and T. F. Jaramillo, Combining theory and experiment in electrocatalysis: Insights into materials design, *Science*, 2017, **355**, eaad4998.
4 F. E. Osterloh and B. A. Parkinson, Recent developments in solar water-splitting photocatalysis, *MRS Bull.*, 2011, **36**, 17–22.
5 P. Slovic, J. H. Flynn and M. Layman, Perceived risk, trust, and the politics of nuclear waste, *Science*, 1991, **254**, 1603–1607.
6 L. Schlapbach and A. Züttel, Hydrogen-storage materials for mobile applications, *Nature*, 2001, **414**, 353–358.
7 W. Cui, Q. Liu, N. Cheng, A. M. Asiri and X. Sun, Activated carbon nanotubes: A highly-active metal-free electrocatalyst for hydrogen evolution reaction, *Chem. Commun.*, 2014, **50**, 9340–9342.
8 J. R. McKone, S. C. Marinescu, B. S. Brunschwig, J. R. Winkler and H. B. Gray, Earth-abundant hydrogen evolution electrocatalysts, *Chem. Sci.*, 2014, **5**, 865–878.
9 S. Anantharaj, S. R. Ede, K. Sakthikumar, K. Karthick, S. Mishra and S. Kundu, Recent trends and perspectives in electrochemical water splitting with an emphasis on sulfide, selenide, and phosphide catalysts of Fe, Co, and Ni: A review, *ACS Catal.*, 2016, **6**, 8069–8097.
10 Y. Wang, B. Kong, D. Zhao, H. Wang and C. Selomulya, Strategies for developing transition metal phosphides as

11544 | *Phys. Chem. Chem. Phys.*, 2021, **23**, 11538–11547

This journal is © the Owner Societies 2021

heterogeneous electrocatalysts for water splitting, *Nano Today*, 2017, **15**, 26–55.

11 F. Davodi, M. Tavakkoli, J. Lahtinen and T. Kallio, Straightforward synthesis of nitrogen-doped carbon nanotubes as highly active bifunctional electrocatalysts for full water splitting, *J. Catal.*, 2017, **353**, 19–27.

12 A. Li, Y. Sun, T. Yao and H. Han, Earth-abundant transition-metal-based electrocatalysts for water electrolysis to produce renewable hydrogen, *Chem. – Eur. J.*, 2018, **24**, 18334–18355.

13 D. Khalafallah, M. Zhi and Z. Hong, Recent trends in synthesis and investigation of nickel phosphide compound/hybrid-based electrocatalysts towards hydrogen generation from water electrocatalysis, *Top. Curr. Chem.*, 2019, **377**, 29.

14 C. Hu, C. Lv, S. Liu, Y. Shi, J. F. Song, Z. Zhang, J. Cai and A. Watanabe, Nickel phosphide electrocatalysts for hydrogen evolution reaction, *Catalysts*, 2020, **10**, 188.

15 M. Ledendecker, H. Schlott, M. Antonietti, B. Meyer and M. Shalom, Experimental and theoretical assessment of Ni-based binary compounds for the hydrogen evolution reaction, *Adv. Energy Mater.*, 2017, **7**, 1601735.

16 V. Vij, S. Sultan, A. M. Harzandi, A. Meena, J. N. Tiwari, W.-G. Lee, T. Yoon and K. S. Kim, Nickel-based electrocatalysts for energy-related applications: Oxygen reduction, oxygen evolution, and hydrogen evolution reactions, *ACS Catal.*, 2017, **7**, 7196–7225.

17 Z. Zhou, L. Wei, Y. Wang, H. E. Karahan, Z. Chen, Y. Lei, X. Chen, S. Zhai, X. Liao and Y. Chen, Hydrogen evolution reaction activity of nickel phosphide is highly sensitive to electrolyte pH, *J. Mater. Chem. A*, 2017, **5**, 20390–20397.

18 A. Ray, S. Sultana, L. Paramanik and K. M. Parida, Recent advances in phase, size, and morphology-oriented nanostructured nickel phosphide for overall water splitting, *J. Mater. Chem. A*, 2020, **8**, 19196–19245.

19 Y. Sun, L. Hang, Q. Shen, T. Zhang, H. Li, X. Zhang, X. Lyu and Y. Li, Mo doped Ni_2P nanowire arrays: An efficient electrocatalyst for the hydrogen evolution reaction with enhanced activity at all pH values, *Nanoscale*, 2017, **9**, 16674–16679.

20 J. L. Lado, X. Wang, E. Paz, E. Carbó-Argibay, N. Guldris, C. Rodríguez-Abreu, L. Liu, K. Kovnir and Y. V. Kolen'ko, Design and synthesis of highly active Al–Ni–P foam electrode for hydrogen evolution reaction, *ACS Catal.*, 2015, **5**, 6503–6508.

21 Y. Zhang, Y. Liu, M. Ma, X. Ren, Z. Liu, G. Du, A. M. Asiri and X. Sun, A Mn-doped Ni_2P nanosheet array: An efficient and durable hydrogen evolution reaction electrocatalyst in alkaline media, *Chem. Commun.*, 2017, **53**, 11048–11051.

22 Z. Jin, P. Li, X. Huang, G. Zeng, Y. Jin, B. Zheng and D. Xiao, Three-dimensional amorphous tungsten-doped nickel phosphide microsphere as an efficient electrocatalyst for hydrogen evolution, *J. Mater. Chem. A*, 2014, **2**, 18593–18599.

23 L. Wen, J. Yu, C. Xing, D. Liu, X. Lyu, W. Cai and X. Li, Flexible vanadium-doped Ni_2P nanosheet arrays grown on carbon cloth for an efficient hydrogen evolution reaction, *Nanoscale*, 2019, **11**, 4198–4203.

24 K. N. Dinh, X. Sun, Z. Dai, Y. Zheng, P. Zheng, J. Yang, J. Xu, Z. Wang and Q. Yan, O_2 plasma and cation tuned nickel phosphide nanosheets for highly efficient overall water splitting, *Nano Energy*, 2018, **54**, 82–90.

25 L. Han, T. Yu, W. Lei, W. Liu, K. Feng, Y. Ding, G. Jiang, P. Xu and Z. Chen, Nitrogen-doped carbon nanocones encapsulating with nickel–cobalt mixed phosphides for enhanced hydrogen evolution reaction, *J. Mater. Chem. A*, 2017, **5**, 16568–16572.

26 Y. Li, J. Liu, C. Chen, X. Zhang and J. Chen, Preparation of NiCoP hollow quasi-polyhedra and their electrocatalytic properties for hydrogen evolution in alkaline solution, *ACS Appl. Mater. Interfaces*, 2017, **9**, 5982–5991.

27 J. Liu, Z. Wang, J. David, J. Llorca, J. Li, X. Yu, A. Shavel, J. Arbiol, M. Meyns and A. Cabot, Colloidal $Ni_{2-x}Co_xP$ nanocrystals for the hydrogen evolution reaction, *J. Mater. Chem. A*, 2018, **6**, 11453–11462.

28 P. Wang, Z. Pu, Y. Li, L. Wu, Z. Tu, M. Jiang, Z. Kou, I. S. Amiinu and S. Mu, Iron-doped nickel phosphide nanosheet arrays: An efficient bifunctional electrocatalyst for water splitting, *ACS Appl. Mater. Interfaces*, 2017, **9**, 26001–26007.

29 Y. Li, H. Zhang, M. Jiang, Q. Zhang, P. He and X. Sun, 3D self-supported Fe-doped Ni_2P nanosheet arrays as bifunctional catalysts for overall water splitting, *Adv. Funct. Mater.*, 2017, **27**, 1702513.

30 H. Huang, C. Yu, C. Zhao, X. Han, J. Yang, Z. Liu, S. Li, M. Zhang and J. Qiu, Iron-tuned super nickel phosphide microstructures with high activity for electrochemical overall water splitting, *Nano Energy*, 2017, **34**, 472–480.

31 C. Lin, D. Wang, H. Jin, P. Wang, D. Chen, B. Liu and S. Mu, Construction of an iron and oxygen co-doped nickel phosphide based on MOF derivatives for highly efficient and long-enduring water splitting, *J. Mater. Chem. A*, 2020, **8**, 4570–4578.

32 M. Hakala and K. Laasonen, Hydrogen adsorption trends on Al-doped Ni_2P surfaces for optimal catalyst design, *Phys. Chem. Chem. Phys.*, 2018, **20**, 13785–13791.

33 L. Partanen, M. Hakala and K. Laasonen, Hydrogen adsorption trends on various metal-doped Ni_2P surfaces for optimal catalyst design, *Phys. Chem. Chem. Phys.*, 2019, **21**, 184–191.

34 J. K. Nørskov, J. Rossmeisl, A. Logadottir, L. Lindqvist, J. R. Kitchin, T. Bligaard and H. Jónsson, Origin of the overpotential for oxygen reduction at a fuel-cell cathode, *J. Phys. Chem. B*, 2004, **108**, 17886–17892.

35 J. K. Nørskov, T. Bligaard, A. Logadottir, J. R. Kitchin, J. G. Chen, S. Pandelov and U. Stimming, Trends in the exchange current for hydrogen evolution, *J. Electrochem. Soc.*, 2005, **152**, J23–J26.

36 J. Greeley, T. F. Jaramillo, J. Bonde, I. Chorkendorff and J. K. Nørskov, Computational high-throughput screening of electrocatalytic materials for hydrogen evolution, *Nat. Mater.*, 2006, **5**, 909–913.

37 M. H. Hansen, L.-A. Stern, L. Feng, J. Rossmeisl and X. Hu, Widely available active sites on Ni_2P for electrochemical

This journal is © the Owner Societies 2021

Phys. Chem. Chem. Phys., 2021, **23**, 11538–11547 | **11545**

hydrogen evolution – insights from first principles calculations, *Phys. Chem. Chem. Phys.*, 2015, **17**, 10823–10829.

38 R. B. Wexler, J. M. P. Martirez and A. M. Rappe, Stable phosphorus-enriched (0001) surfaces of nickel phosphides, *Chem. Mater.*, 2016, **28**, 5365–5372.

39 Q. Li and X. Hu, First-principles study of Ni$_2$P(0001) surfaces, *Phys. Rev. B: Condens. Matter Mater. Phys.*, 2006, **74**, 035414.

40 Y.-H. Chung, K. Gupta, J.-H. Jang, H. S. Park, I. Jang, J. H. Jang, Y.-K. Lee, S.-C. Lee and S. J. Yoo, Rationalization of electrocatalysis of nickel phosphide nanowires for efficient hydrogen production, *Nano Energy*, 2016, **26**, 496–503.

41 J. VandeVondele, M. Krack, F. Mohamed, M. Parrinello, T. Chassaing and J. Hutter, QUICKSTEP: Fast and accurate density functional calculations using a mixed Gaussian and plane waves approach, *Comput. Phys. Commun.*, 2005, **167**, 103–128.

42 J. Hutter, M. Iannuzzi, F. Schiffmann and J. VandeVondele, cp2k: Atomistic simulations of condensed matter systems, *Wiley Interdiscip. Rev.: Comput. Mol. Sci.*, 2014, **4**, 15–25.

43 J. P. Perdew, K. Burke and M. Ernzerhof, Generalized gradient approximation made simple, *Phys. Rev. Lett.*, 1996, **77**, 3865–3868.

44 S. Goedecker, M. Teter and J. Hutter, Separable dual-space Gaussian pseudopotentials, *Phys. Rev. B: Condens. Matter Mater. Phys.*, 1996, **54**, 1703–1710.

45 C. Hartwigsen, S. Goedecker and J. Hutter, Relativistic separable dual-space Gaussian pseudopotentials from H to Rn, *Phys. Rev. B: Condens. Matter Mater. Phys.*, 1998, **58**, 3641–3662.

46 M. Krack, Pseudopotentials for H to Kr optimized for gradient-corrected exchange–correlation functionals, *Theor. Chem. Acc.*, 2005, **114**, 145–152.

47 P. Haas, F. Tran and P. Blaha, Calculation of the lattice constant of solids with semilocal functionals, *Phys. Rev. B: Condens. Matter Mater. Phys.*, 2009, **79**, 085104.

48 A. H. Reshak and M. Jamal, Calculation of the lattice constant of hexagonal compounds with two dimensional search of equation of state and with semilocal functionals a new package (2D-optimize), *J. Alloys Compd.*, 2013, **555**, 362–366.

49 F. Tran, R. Laskowski, P. Blaha and K. Schwarz, Performance on molecules, surfaces, and solids of the Wu-Cohen GGA exchange–correlation energy functional, *Phys. Rev. B: Condens. Matter Mater. Phys.*, 2007, **75**, 115131.

50 S. Grimme, J. Antony, S. Ehrlich and H. Krieg, A Consistent and accurate *ab initio* parametrization of density functional dispersion correction (DFT-D) for the 94 elements H-Pu, *J. Chem. Phys.*, 2010, **132**, 154104.

51 S. Grimme, S. Ehrlich and L. Goerigk, Effect of the damping function in dispersion corrected density functional theory, *J. Comput. Chem.*, 2011, **32**, 1456–1465.

52 R. B. Wexler, J. M. P. Martirez and A. M. Rappe, Active role of phosphorus in the hydrogen evolving activity of nickel phosphide(0001) surfaces, *ACS Catal.*, 2017, **7**, 7718–7725.

53 A. B. Hernandez, H. Ariga, S. Takakusagi, K. Kinoshita, S. Suzuki, S. Otani, S. T. Oyama and K. Asakura, Dynamical LEED analysis of Ni$_2$P(0001)-1 × 1: Evidence for P-covered surface structure, *Chem. Phys. Lett.*, 2011, **513**, 48–52.

54 D. Kanama, S. T. Oyama, S. Otani and D. F. Cox, Photoemission and LEED characterization of Ni$_2$P(0001), *Surf. Sci.*, 2004, **552**, 8–16.

55 M. G. Moula, S. Suzuki, W.-J. Chun, S. Otani, S. T. Oyama and K. Asakura, Surface structures of Ni$_2$P(0001)-scanning tunneling microscopy (STM) and low-energy electron diffraction (LEED) characterizations, *Surf. Interface Anal.*, 2006, **38**, 1611–1614.

56 S. Suzuki, G. M. Moula, T. Miyamoto, Y. Nakagawa, K. Kinosthita, K. Asakura, S. T. Oyama and S. Otani, Scanning tunneling microscopy and photoemission electron microscopy studies on single crystal Ni$_2$P surfaces, *J. Nanosci. Nanotechnol.*, 2009, **9**, 195–201.

57 D. Guo, Y. Nakagawa, H. Ariga, S. Suzuki, K. Kinoshita, T. Miyamoto, S. Takakusagi, K. Asakura, S. Otani and S. T. Oyama, STM studies on the reconstruction of the Ni$_2$P (10$\bar{1}$0) surface, *Surf. Sci.*, 2010, **604**, 1347–1352.

58 H. Ariga, M. Kawashima, S. Takakusagi and K. Asakura, Density function theoretical investigation on the Ni$_3$PP structure and the hydrogen adsorption property of the Ni$_2$P(0001) surface, *Chem. Lett.*, 2013, **42**, 1481–1483.

59 P. Liu, J. A. Rodriguez, T. Asakura, J. Gomes and K. Nakamura, Desulfurization reactions on Ni$_2$P(001) and α-Mo$_2$C(001) surfaces: Complex role of P and C sites, *J. Phys. Chem. B*, 2005, **109**, 4575–4583.

60 J. A. Rodriguez, J.-Y. Kim, J. C. Hanson, S. J. Sawhill and M. E. Bussell, Physical and chemical properties of MoP, Ni$_2$P, and MoNiP hydrodesulfurization catalysts: Time-resolved X-ray diffraction, density functional, and hydrodesulfurization activity studies, *J. Phys. Chem. B*, 2003, **107**, 6276–6285.

61 B. Hammer, L. B. Hansen and J. K. Nørskov, Improved adsorption energetics within density-functional theory using revised Perdew–Burke–Ernzerhof functionals, *Phys. Rev. B: Condens. Matter Mater. Phys.*, 1999, **59**, 7413–7421.

62 E. Skúlason, G. S. Karlberg, J. Rossmeisl, T. Bligaard, J. Greeley, H. Jónsson and J. K. Nørskov, Density functional theory calculations for the hydrogen evolution reaction in an electrochemical double layer on the Pt(111) electrode, *Phys. Chem. Chem. Phys.*, 2007, **9**, 3241–3250.

63 P. Liu and J. A. Rodriguez, Catalysts for hydrogen evolution from the [NiFe] hydrogenase to the Ni$_2$P(001) surface: The importance of ensemble effect, *J. Am. Chem. Soc.*, 2005, **127**, 14871–14878.

64 Y. Lu, Y. Deng, S. Lu, Y. Liu, J. Lang, X. Cao and H. Gu, MOF-derived cobalt–nickel phosphide nanoboxes as electrocatalysts for the hydrogen evolution reaction, *Nanoscale*, 2019, **11**, 21259–21265.

65 B. Ma, Z. Yang, Y. Chen and Z. Yuan, Nickel cobalt phosphide with three-dimensional nanostructure as a highly efficient electrocatalyst for hydrogen evolution reaction in both acidic and alkaline electrolytes, *Nano Res.*, 2019, **12**, 375–380.

66 H.-W. Man, C.-S. Tsang, M. M.-J. Li, J. Mo, B. Huang, L. Y. S. Lee, Y.-C. Leung, K.-Y. Wong and S. C. E. Tsang, Transition metal-doped nickel phosphide nanoparticles as

11546 | *Phys. Chem. Chem. Phys.*, 2021, **23**, 11538–11547

This journal is © the Owner Societies 2021

electro- and photocatalysts for hydrogen generation reactions, *Appl. Catal., B*, 2019, **242**, 186–193.

67 Y. Pan, Y. Chen, Y. Lin, P. Cui, K. Sun, Y. Liu and C. Liu, Cobalt nickel phosphide nanoparticles decorated carbon nanotubes as advanced hybrid catalysts for hydrogen evolution, *J. Mater. Chem. A*, 2016, **4**, 14675–14686.

68 B. Zhang, J. Zhang, X. Tang, Y. H. Lui and S. Hu, An investigation of Fe incorporation on the activity and stability of homogeneous $(Fe_xNi_{1-x})_2P$ solid solutions as electrocatalysts for alkaline hydrogen evolution, *Electrochim. Acta*, 2019, **294**, 297–303.

69 W. L. Kwong, C. C. Lee and J. Messinger, Scalable two-step synthesis of nickel–iron phosphide electrodes for stable and efficient electrocatalytic hydrogen evolution, *J. Phys. Chem. C*, 2017, **121**, 284–292.

70 Y. Du, Z. Li, Y. Liu, Y. Yang and L. Wang, Nickel–iron phosphides nanorods derived from bimetallic–organic frameworks for hydrogen evolution reaction, *Appl. Surf. Sci.*, 2018, **457**, 1081–1086.

71 Q. Zhou, Z. Chen, L. Zhong, X. Li, R. Sun, J. Feng, G.-C. Wang and X. Peng, Solvothermally controlled synthesis of organic–inorganic hybrid nanosheets as efficient pH-universal hydrogen-evolution electrocatalysts, *ChemSusChem*, 2018, **11**, 2828–2836.

72 M. Guo, Y. Qu, F. Zeng and C. Yuan, Synthetic strategy and evaluation of hierarchical nanoporous NiO/NiCoP microspheres as efficient electrocatalysts for hydrogen evolution reaction, *Electrochim. Acta*, 2018, **292**, 88–97.

73 H. Zheng, X. Huang, H. Gao, G. Lu, A. Li, W. Dong and G. Wang, Cobalt-tuned nickel phosphide nanoparticles for highly efficient electrocatalysis, *Appl. Surf. Sci.*, 2019, **479**, 1254–1261.

74 S. Surendran, S. Shanmugapriya, A. Sivanantham, S. Shanmugam and R. Kalai Selvan, Electrospun carbon nanofibers encapsulated with NiCoP: A multifunctional electrode for supercapattery and oxygen reduction, oxygen evolution, and hydrogen evolution reactions, *Adv. Energy Mater.*, 2018, **8**, 1800555.

This journal is © the Owner Societies 2021

Phys. Chem. Chem. Phys., 2021, **23**, 11538–11547 | 11547